Applied Catalysis B: Environmental 125 (2012) 492–498

Contents lists available at SciVerse ScienceDirect

Applied Catalysis B: Environmental

journal homepage: www.elsevier.com/locate/apcatb

Catalytic decomposition of N_2O over $Cu_xCe_{1-x}O_y$ mixed oxides

Haibo Zhou, Zhen Huang, Chao Sun, Feng Qin, Desheng Xiong, Wei Shen*, Hualong Xu*

Department of Chemistry, Shanghai Key Laboratory of Molecular Catalysis and Innovative Materials, Laboratory of Advanced Materials, Fudan University, Shanghai 200433, PR China

ARTICLE INFO

Article history:
Received 8 November 2011
Received in revised form 16 June 2012
Accepted 20 June 2012
Available online 27 June 2012

Keywords:
Synergetic effect
N_2O decomposition
$Cu_xCe_{1-x}O_y$ catalyst
In situ DRIFTS

ABSTRACT

The catalytic N_2O decomposition was investigated over a series of $Cu_xCe_{1-x}O_y$ mixed oxides with different Cu/Ce molar ratios. Effects of synergy over mixed oxides of CeO_2 and CuO were observed significantly, the catalyst of $Cu_{0.67}Ce_{0.33}O_y$ exhibited the high activity among the Cu–Ce–O mixed oxides for N_2O decomposition. Characterizations of XRD, N_2-adsorption, XPS, and H_2-TPR were applied to correlate their properties with the corresponding catalytic performance, and reveal the synergetic effect between CuO and CeO_2 for N_2O decomposition. In situ DRIFTS investigation confirmed the presence of Cu^I species that was closely related with the activity of $Cu_xCe_{1-x}O_y$ catalyst. The synergy of $Cu_xCe_{1-x}O_y$ promoted the stability and the ability to regenerate the active Cu^I site.

1. Introduction

Nitrous oxide (N_2O) is a strong greenhouse gas, which shows 310 and 21 times of the global warming potential (GWP) as compared to those of CO_2 and CH_4, respectively. Furthermore, it contributes to the stratospheric ozone destruction [1,2]. The concentration of N_2O in the atmosphere is increasing by 0.2–0.3% per year, which is mainly caused by anthropogenic activities such as chemical manufacture and energy production [2,3]. Thus, the reduction of anthropogenic N_2O emissions is urgently required. Several methods, such as reduction [4], thermal and catalytic N_2O decomposition [5], have been studied recently. Among these methods, direct catalytic N_2O decomposition is considered the most effective and economic one.

Various types of catalysts have been prepared for N_2O catalytic decomposition, such as: Ru/Al_2O_3, Co_3O_4, $Fe_xCe_{1-x}O_2$, $LaCoO_3$, Fe-ZSM-5, and Cu-ZSM-5 [6–11]. Noble metals supported on SBA-15 or Al_2O_3, such as Rh and Ru, exhibited excellent catalytic performance [5]. Considering economic cost, the non-noble metal oxides are of great potential for the industrial application [3]. It was reported that the mixed oxides could show remarkable advantage in catalytic decomposition of N_2O compared to the pure oxides [8,12]. Perez-Alonso et al. [8] reported that $Fe_{0.5}Ce_{0.5}O_2$ showed the best activity among the Fe–Ce–O mixed oxides. He Hong group also reported that the introduction of CeO_2 into the Co_3O_4 spinel could promote the catalytic activity [12]. The authors attributed the improvement of catalytic activity over mixed oxides to the larger surface area and better redox property led by the synergetic effect.

Cu-based catalysts are widely applied in industry. It was reported that Cs-doped CuO [13], $YBa_2Cu_3O_7$, Nd_2CuO_4 [14,15] and Cu-containing zeolites (ZSM-5, Y, Beta, etc.) [16] were active for N_2O decomposition, in which Cu^I ion acted as the active center [14,17]. Meanwhile, it was reported that CeO_2 could improve the activity of CuO in the selective oxidation of CO [18], soot oxidation [19], and the water-gas shift (WGS) reaction [20]. Nevertheless, the performance of $Cu_xCe_{1-x}O_y$ mixed oxides on catalytic N_2O decomposition has not been studied. In the present work, we synthesize a series of $Cu_xCe_{1-x}O_y$ mixed oxides with different Cu/Ce molar ratios, and focus on the impact of the synergetic effect between Cu and Ce on the catalytic performance. In situ DRIFTS method served as a powerful tool to detect the surface Cu^I species and reveal the correlation between the composition of $Cu_xCe_{1-x}O_y$ and the catalytic activity.

2. Experimental

2.1. Catalysts preparation

A series of $Cu_xCe_{1-x}O_y$ mixed oxide catalysts with mole percentage of 100, 80, 67, 50, 20, and 0 Cu metal (Ce balance) were prepared by citrate acid method [21]. Stoichiometric amounts of analytical purity grade of $Cu(NO_3)_2{\cdot}3H_2O$, and $Ce(NO_3)_3{\cdot}6H_2O$ were mixed in an aqueous solution. Citric acid was then added to the mixture (citric acid: (Ce + Cu) = 2:1 (molar ratio)) under continuous stirring until the solid was dissolved. The solution was heated at 80 °C to remove water until a viscous gel was formed. The gel was dried overnight in an oven at 120 °C, and amorphous precursor was

* Corresponding authors. Tel.: +86 21 65642401; fax: +86 21 65641740.
E-mail addresses: wshen@fudan.edu.cn (W. Shen), shuhl@fudan.edu.cn (H. Xu).

0926-3373/$ – see front matter © 2012 Elsevier B.V. All rights reserved.
http://dx.doi.org/10.1016/j.apcatb.2012.06.021

obtained. The precursor was calcined at 450 °C for 5 h to obtain the mixed oxide. The as-synthesized mixed oxides were denoted as $Cu_xCe_{1-x}O_y$.

2.2. Catalysts characterization

XRD patterns were recorded with a Bruker D4 powder X-ray diffractometer, which employed Ni-filtered Cu Kα radiation (λ = 1.5418 Å) and was operated at 40 kV and 40 mA. Diffraction patterns were recorded with scan step of 0.02° at the speed of 0.2 s/step for 2θ between 5 and 80°.

Nitrogen adsorption–desorption isotherms at 77 K were performed using a Micromeritics TRISTAR 3000 apparatus. The samples were degassed at 120 °C and high vacuum prior to the measurements. BET model was used to estimate the surface area of the materials.

X-ray photoelectron spectroscopy (XPS) data were carried out with a Perkin Elmer PHI 5000C system equipped with a hemispherical electron energy analyzer. The carbonaceous C 1s line (284.6 eV) was used as the reference to calibrate the binding energy (BE).

H_2-temperature programmed reduction (TPR) was carried out in Micromeritics AutoChem II 2920, equipped with a quartz U-tube reactor coupled to a TCD detector for analyzing the H_2 consumption. Before the test, the sample was pretreated in helium stream at 100 °C for 30 min, then the temperature cooled down to 50 °C in helium, and stabilized for 30 min. After that, a H_2–Ar mixture (10% H_2 by volume) with a flow rate of 50 mL min^{-1} was switched on, and the temperature was increased within the range of 50–550 °C (heating rate = 5 °C min^{-1}).

The diffuse reflectance infrared Fourier transform spectra (DRIFTS) were recorded on a FTIR (Nicolet 6700) spectrometer equipped with a high-sensitive MCT detector cooled by liquid nitrogen. The DRIFTS cell (Harrick) was fitted with CaF_2 windows and a heating cartridge that allowed samples to be heated to 700 °C. Samples were activated in helium at 20, 100, 200 and 400 °C for 1 h, and then cooled to 20 °C under a helium flow of 20 mL min^{-1}. Spectra of adsorbates were collected after treated in the flow of 0.5 vol.% CO–He mixture for 30 min. All spectra were measured at the respective temperatures and under continuous flow of gas, with resolution of 4 cm^{-1} and accumulation of 100 scans.

2.3. Activity tests

The activity tests for N_2O catalytic decomposition were carried out in an automated eight flow reactor system. The catalysts with particle sizes of 40–60 mesh were packed in the isothermal part of the quartz tubular reactor. Prior to the reaction, all the samples were pretreated in a He flow at 400 °C for 1 h, then, the temperature was cooled down to 250 °C. The pressure was set to 0.3 MPa and the concentration of N_2O was 2600 ppm balanced by helium with the total GHSV at 19,000 h^{-1}. The reaction temperature was from 250 to 550 °C. At each temperature the reactions were stabilized for 30 min before analysis. The products were automatically sampled and analyzed by Finnigan Trace GC Ultra equipped with a thermal conductivity detector (TCD), with a 10 m Poraplot Q capillary column.

3. Results and discussion

3.1. Textural properties of $Cu_xCe_{1-x}O_y$ catalyst

XRD patterns of $Cu_xCe_{1-x}O_y$ samples are shown in Fig. 1A. New crystal phase diffraction peaks were not clearly detected except those for CuO (JPCDS card PDF 80-1917) and CeO_2 (JPCDS card PDF 81-0792). Noticeably, CuO phase cannot be observed in XRD pattern of $Cu_{0.2}Ce_{0.8}O_y$, indicating that CuO phase is either amorphous, or incorporating to the ceria to form a solid solution. The average crystal size of CuO and CeO_2 in $Cu_xCe_{1-x}O_y$ mixed oxides remain constant indicated by the calculation with Scherrer's equation (listed in Table 1). Meanwhile, the surface area of the mixed oxides increases compared to the CuO.

Table 1
Physicochemical properties of the $Cu_xCe_{1-x}O_y$ catalysts.

Catalyst	Surface area (m^2 g^{-1})	Size of CuO[a] (nm)	Size of CeO_2[b] (nm)	Peak area[c] (a.u.)
CuO	1	29	–	23
$Cu_{0.8}Ce_{0.2}O_y$	31	25	–	227
$Cu_{0.67}Ce_{0.33}O_y$	45	24	9	485
$Cu_{0.5}Ce_{0.5}O_y$	67	26	7	267
$Cu_{0.2}Ce_{0.8}O_y$	55	–	6	137
CeO_2	42	–	11	–

[a] Calculated from the CuO phase (2θ = 35.4°) using the Scherrer's equation.
[b] Calculated from the CeO_2 phase (2θ = 28.5°) using the Scherrer's equation.
[c] Areas of the IR peak of Cu^I–CO at 2100 cm^{-1}.

Furthermore, it is found that the diffraction peak of CuO (0 0 2) shifts toward lower angle with the introduction of CeO_2 (see the detail in Fig. 1B), indicating the expansion of the CuO lattice. However, changes in the CeO_2 (1 1 1) were not detected (see the detail in Fig. 1C).

It was reported that Cu could substitute Ce into the CeO_2 cell and reduce the CeO_2 cell size [22]. Nonetheless, the contraction was not detected in our catalysts. Djinovic et al. [20] suggested that the increasing amount of reduced Ce^{3+} could expand the CeO_2 cell dimension; and, the coexistence of these two opposite effects in the solid solution lead the negligible changes in the CeO_2 cell size. As for the CuO lattice, the strong interaction between copper and cerium may promote the electron interaction between Cu^{2+} and Ce^{3+} (Cu^{2+} (0.072 nm) + Ce^{3+} → Cu^{+} (0.096 nm) + Ce^{4+}). Hence, the synergetic effect enriches electron density of Cu in the mixed oxides, expands the CuO cell, and shifts CuO (0 0 2) diffraction signal toward lower angle.

The XPS results of the $Cu_xCe_{1-x}O_y$ catalysts are illustrated in Fig. 2. The pure oxide CuO presents a peak at 933.9 eV, together with a strong shake-up peak from 941.4 to 944.2 eV, which could be ascribed to bulk CuO [23]. While, for the mixed oxides, the shake-up peak disappears; in addition, the Cu_{2p} BE of all mixed oxides declines with the introduction of the CeO_2. For instance, the binding energy of $Cu_{0.2}Ce_{0.8}O_y$ decreases by 1.9 eV, which suggests a change in the electronic state of Cu, and the Cu—O bond, is weakened.

It's reported that the reducibility enhancement of metal oxides can effectively promote the activity of catalytic N_2O decomposition [13,24]. In this case, the weakened Cu—O bond justifies the boosted activity for the mixed oxides system: the synergetic effect weakens the bond between Cu and O and enhances the reducibility of CuO in mixed oxides.

It's believed that the weakened Cu—O bond could be reduced by H_2 at low temperature [13]. Meanwhile, active site (such as Fe [8], Co [12], and Cu [13]) exhibits better reducibility would show better performance in the decomposition of N_2O. So, the enhancement of reducibility in mixed oxides is visualized by H_2-TPR. Fig. 3 compared the H_2-TPR profiles of the $Cu_xCe_{1-x}O_y$ samples. CeO_2 gives a weak reduction peak appeared at 440 °C, which could be ascribed to the reduction of surface capping oxygen in CeO_2. While, this peak is not observed in the Cu-containing catalysts [22]. The pure oxide CuO gives two reduction peaks appeared at 180 and 215 °C. The $Cu_{0.2}Ce_{0.8}O_y$, displays reduction peaks between 90 and 150 °C, in which all the CuO phase close interact with CeO_2 leading to the decrease in the reduction temperature of CuO [18,25]. H_2-TPR of $Cu_xCe_{1-x}O_y$ mixed oxide can be divided in two parts [26]: zone (I) corresponds to the reduction of CuO which has strong synergic

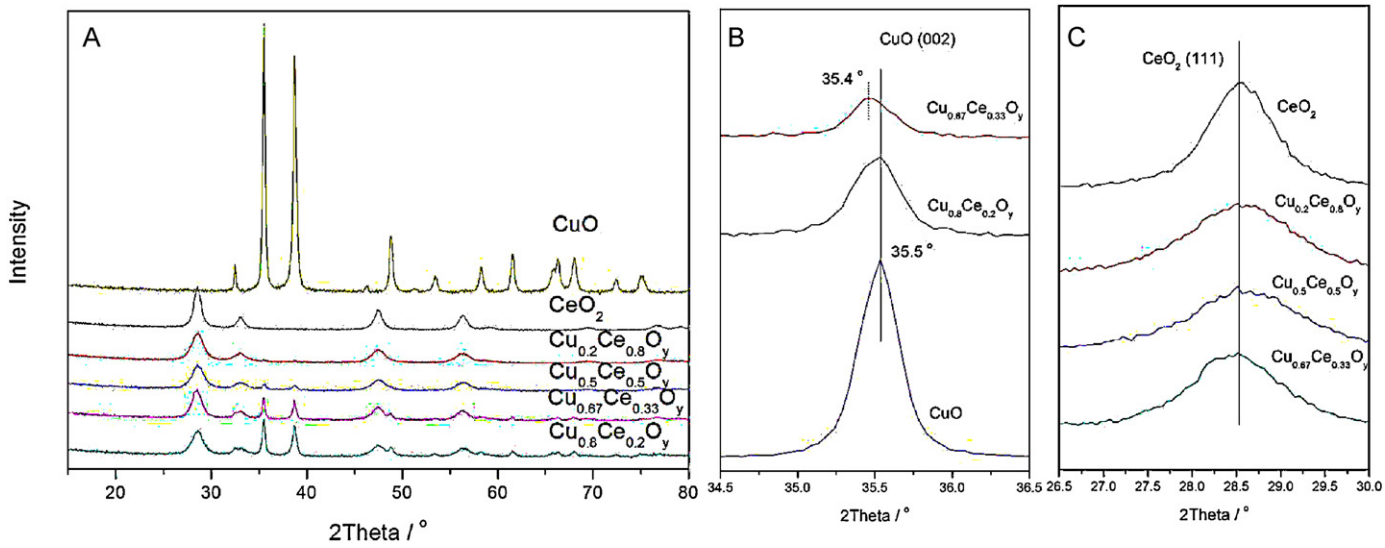

Fig. 1. (A) XRD patterns of $Cu_xCe_{1-x}O_y$ catalysts. (B) amplification of the (0 0 2) reflection for CuO. (C) Amplification of the (1 1 1) reflection for CeO_2.

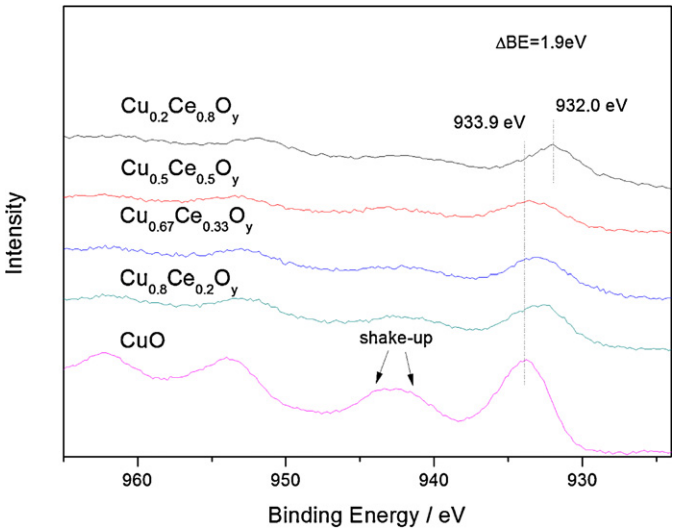

Fig. 2. XPS region spectra of Cu_{2p} obtained on $Cu_xCe_{1-x}O_y$ samples.

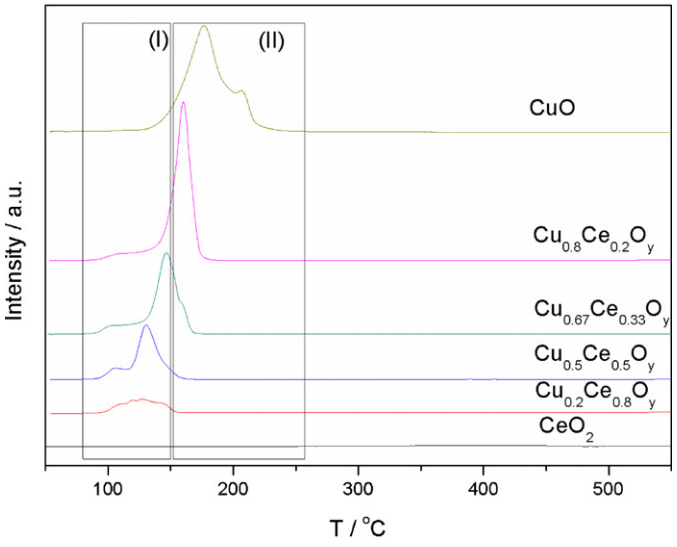

Fig. 3. H_2-TPR profiles of CuO-CeO_2 mixed oxides catalysts. Conditions: 10 vol.% H_2–Ar 50 mL min^{-1} and ramping rate of 5 °C min^{-1}.

effect with CeO_2, whereas zone (II) corresponds to the reduction of the Cu species without interaction with CeO_2. It was reported that Cu species, which could be reduced in the low temperature range, exhibited prominent activity in the low temperature oxidation of CO [25]. Thus, it is reasonably speculated that the active sites are mainly provided by the Cu species which can be reduced in zone (I).

It is noteworthy to find that the reduction peaks shift to higher temperature and the corresponding intensity raises with the increasing proportion of CuO within the mixed oxide. For the $Cu_{0.2}Ce_{0.8}O_y$ and $Cu_{0.5}Ce_{0.5}O_y$, nearly all H_2 consumption is located in the zone (I). As the amount of CuO reaches up to 80%, most of Cu species do not have strong interaction with CeO_2, so that it cannot be reduced in the low temperature range. The pure oxide CuO requires even higher reduction temperature than the $Cu_xCe_{1-x}O_y$ mixed oxide.

To compare the amount of Cu that could be reduced in the zone (I); Table 2 summarizes the amount of CuO in the zone (I), and zone (II). It can be observed that all Cu species in $Cu_{0.2}Ce_{0.8}O_y$ is located in the zone (I), but the total amount of active Cu species in $Cu_{0.2}Ce_{0.8}O_y$ is limited because of the low Cu concentration (8.3 wt.%). With the increasing Cu concentration, more active Cu species is obtained and CuO is partially reduced in the Zone (II). Considering their higher Cu content, $Cu_{0.5}Ce_{0.5}O_y$ and $Cu_{0.67}Ce_{0.33}O_y$ contain considerable amount of highly active Cu species. When the Cu/Ce ratio is higher than 4, most of CuO is reduced in the Zone (II), so $Cu_{0.8}Ce_{0.2}O_y$ and CuO contain little highly active Cu species.

3.2. DRIFTS

To understand the decomposition process of N_2O, the mechanism has been studied by several groups. Fanning and Vannice [17]

Table 2
The H_2 consumption of the Cu species over $Cu_xCe_{1-x}O_y$ catalysts.

Catalysts	H_2 consumption (a.u.)		Weight percentage (%)	
	In zone(I)	In zone(II)	$Cu_{zone(I)}/Cu_{zone(I)+(II)}$	$Cu_{zone(I)}$/catalyst
CeO_2	–	–	–	–
$Cu_{0.2}Ce_{0.8}O_y$	0.74	0.01	99	8.2
$Cu_{0.5}Ce_{0.5}O_y$	1.56	0.08	95	24
$Cu_{0.67}Ce_{0.33}O_y$	2.00	0.86	70	27
$Cu_{0.8}Ce_{0.2}O_y$	0.86	2.88	23	12
CuO	0.35	5.97	5.5	4.4

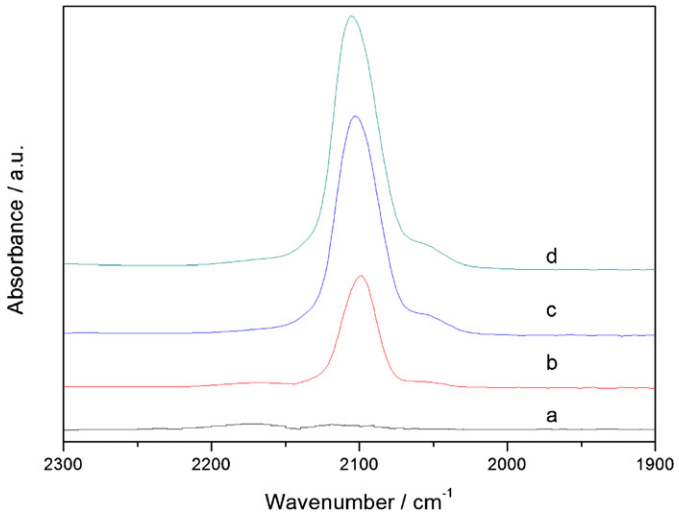

Fig. 4. DRIFTs spectra of adsorbates produced from the flow of 0.5 vol.% CO at 20 °C after activated in helium at different temperature over $Cu_{0.2}Ce_{0.8}O_y$. (a) Activated in helium at 20 °C for 1 h, (b) activated in helium at 100 °C for 1 h, (c) activated in helium at 200 °C for 1 h, (d) activated in helium at 400 °C for 1 h; then cooled to 20 °C in the flow of helium.

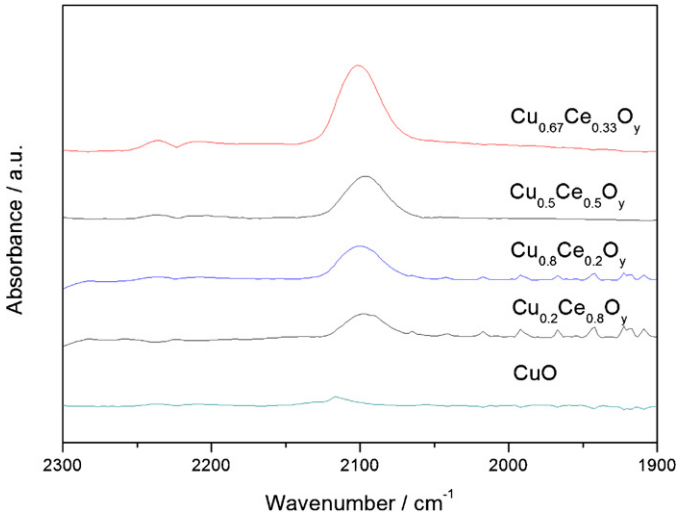

Fig. 5. Infrared spectra recorded of adsorbed CO on the CuO–CeO_2 mixed oxides.

suggested that Cu^I ion at Si—O^- Cu^I sites perform as the active site in the N_2O decomposition. Dandekar and Vannice [4] considered that a balance between Cu^I and Cu^{II} was required in the redox mechanism. Gao and Au [14] also reported that Cu^I act as the active center over fresh $YBa_2Cu_3O_7$. Therefore, it is important to detect and measure the amount of Cu^I active sites for the N_2O decomposition over Cu based catalysts.

In spite of providing some evidence for the synergic effect between CuO and CeO_2, H_2-TPR fails to reveal the difference between Cu^I and Cu^{II}. Instead, IR is a powerful method to propose the mechanism and identify the active sites [27–31]. It provides feasibility to investigate the catalytic decomposition of N_2O in situ, and is used to monitor Cu^I in the presence of CO because CO can be adsorbed on Cu^I and give an adsorption band at 2100 cm^{-1}. In order to avoid the reaction between CO and Cu cations, adsorption is performed at 20 °C [32,33].

Fig. 4 exhibited the IR spectra of CO adsorbed on $Cu_{0.2}Ce_{0.8}O_y$ at 20 °C, through activation under helium at different temperature. No adsorbed CO peak is detected in the spectra of the sample pretreated at 20 °C, indicating that CO cannot be adsorbed on Cu^{II}, and cannot reduce the Cu^{II} component at 20 °C. After thermal treatment at 100 °C, a strong absorption band at 2100 cm^{-1} ascribed to the Cu^I–CO complexes [30,34] appears in the spectra. Moreover, these bands increase in intensity as the activation temperature is raised from 100 to 400 °C. It is believed that Cu^{II} could get an electron from Ce^{III} [27,35], and the activation treatment establishes this sort of close interaction between CuO and CeO_2. The increasing of intensity of the Cu^I–CO complexes can also be observed in other Cu–Ce–O mixed oxides of this series.

These results indicate that (i) in the CuO–CeO_2 mixed oxides, Cu^{II} cannot be reduced by CO at 20 °C and Cu^I does not exist until being heated, (ii) the higher temperature facilitates the yield of Cu^I species.

To investigate the relationship between the amount of Cu^I and the composition of CuO–CeO_2 mixed oxides, we tested the samples reacting with N_2O at 400 °C for 1 h, and then cooled down to 20 °C in helium. Fig. 5 compares the spectra of CO adsorption on CuO-CeO_2 catalysts (diluted with KBr) with different proportion of CuO.

The spectra of CO adsorption on Ce-containing mixed oxides shows strong signals, while the CuO only gives a weak adsorption peak of Cu^+–CO at 2139 cm^{-1}. The amount of adsorbed CO is listed as follows: $Cu_{0.67}Ce_{0.33}O_y > Cu_{0.5}Ce_{0.5}O_y \approx Cu_{0.8}Ce_{0.2}O_y > Cu_{0.2}Ce_{0.8}O_y > CuO$ (see Table 1). As Ce could stabilize Cu^I on the surface of CeO_2 [25], therefore, the synergic effect between Cu and Ce eases the formation of the Cu^I species and stabilize it when cooled to 20 °C. In contrast, for the pure oxide CuO, only a very small peak of Cu^I–CO is detected without CeO_2's stabilization.

In our test, the signals at 1620, 1563, 1283, and 1246 cm^{-1}, that are assigned to the bridging bidentate nitrate, chelating bidentate nitrate, linear nitrite, chelating nitro [36] respectively, are not detected. Thus, N_2O decomposition via these intermediates appearing on the surface of the catalysts can be ruled out.

3.3. Catalytic performance

The conversion of N_2O as a function of temperature using CuO–CeO_2 mixed oxides as catalysts is shown in Fig. 6, and the T_{50} and T_{100} (at which temperature 50% and 100% N_2O decomposition conversion is achieved) are shown in Fig. 7. It is found that CeO_2 is unsuitable for N_2O decomposition. Its T_{50} is about 530 °C, and it is not able to decompose N_2O completely in our test temperature range. In comparison, CuO is more active than

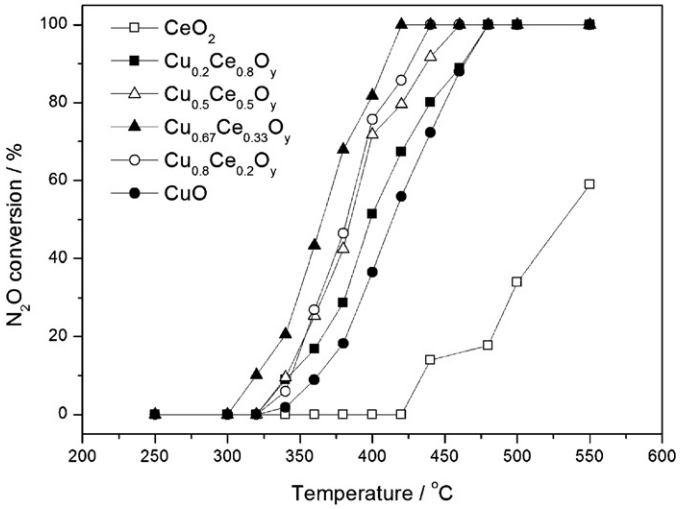

Fig. 6. Conversion of N_2O over different $Cu_xCe_{1-x}O_y$ catalysts Conditions: 2600 ppm N_2O, balance He, P = 0.3 MPa, GHSV = 19,000 h^{-1}.

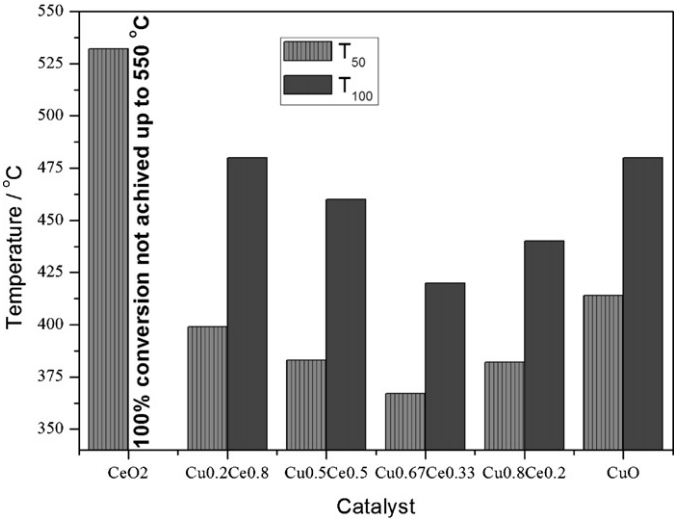

Fig. 7. The T_{50} and T_{100} of different $Cu_xCe_{1-x}O_y$ catalysts (100% N_2O decomposition is not achieved on CeO_2 within reaction tmperature range).

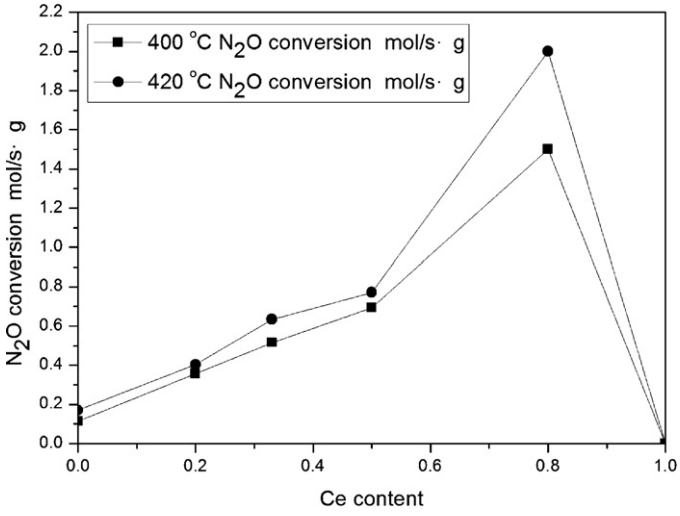

Fig. 9. N_2O conversion rate on one gram Cu at 400 and 420 °C as mmol/(s g) as a function of the Ce content.

CeO_2 for N_2O decomposition, and 100% conversion is achieved at 480 °C. Among the CuO–CeO_2 mixed oxides, $Cu_{0.67}Ce_{0.33}O_y$ shows the best performance for N_2O decomposition, the activity rises rapidly at relatively low temperature and reaches complete N_2O decomposition at 420 °C. $Cu_{0.8}Ce_{0.2}O_y$ and $Cu_{0.5}Ce_{0.5}O_y$ shows similar conversion in all temperature range in our tests. $Cu_{0.2}Ce_{0.8}O_y$ with the lowest Cu-concentration exhibited higher activity than pure CuO.

As shown in Fig. 8, the CuO–CeO_2 mixed oxides exhibited much better stability than the pure metal oxide CuO. The N_2O conversion maintained 100% only for 5 h over CuO catalyst, and then dropped to 15% N_2O conversion rapidly. In contrast, N_2O can be completely decomposed for 80 h over $Cu_{0.67}Ce_{0.33}O_y$ catalyst owing to the stabilization of Cu^I active centers.

Fig. 9 compares the N_2O conversion rate on one gram of Cu at the temperature of 400 and 420 °C. At these temperatures, CeO_2 cannot decompose N_2O. However, with the increasing amount of CeO_2, the N_2O conversion rate increases; and in all of our catalysts, $Cu_{0.2}Ce_{0.8}O_y$ shows the best N_2O conversion rate per one gram of Cu. Combined with the data of XRD and H_2-TPR, it is observed that there is strong synergy between CuO and CeO_2, which could promote the generation of highly active CuO species. Thus, the $Cu_{0.2}Ce_{0.8}O_y$ sample, with the strongest synergetic effect between CuO and CeO_2, exhibits the best N_2O conversion rate on per gram of Cu. However, comparatively scant amount of Cu species limits its conversion rate on per gram of catalyst.

With the increasing Cu/Ce ratio, the amount of Cu reduced in the Zone (I) increases. Specifically, when the Cu/Ce ratio equals to 1 and 2, the $Cu_{0.5}Ce_{0.5}O_y$ and $Cu_{0.67}Ce_{0.33}O_y$ contain considerable amount of active Cu species. However, too much Cu will lead to the formation of inactive Cu species, due to the weak synergetic effect between CuO and CeO_2. The result of catalytic performance indicates that the Cu species with better reducibility plays an important role in determining its activity. Evidenced by the result of H_2-TPR, the reducibility of CuO is enhanced by the synergetic effect between CuO and CeO_2. Meanwhile, as CuO enters the cell of CeO_2, during the heating process, electron migration or oxygen migration may occur in the catalysts where Cu^{II} ions are close to the Ce^{III} ions. In this way, Cu^{II} ions are reduced to Cu^I, and the synergic effect between CuO and CeO_2 stabilize Cu^I centers. DRIFTS results indicate that the mixed oxides with higher proportion of Cu species tend to be reduced at low temperature, and larger number of Cu^I active centers can be formed. Catalytic activity performance correlates well with the amount of Cu^I in catalysts.

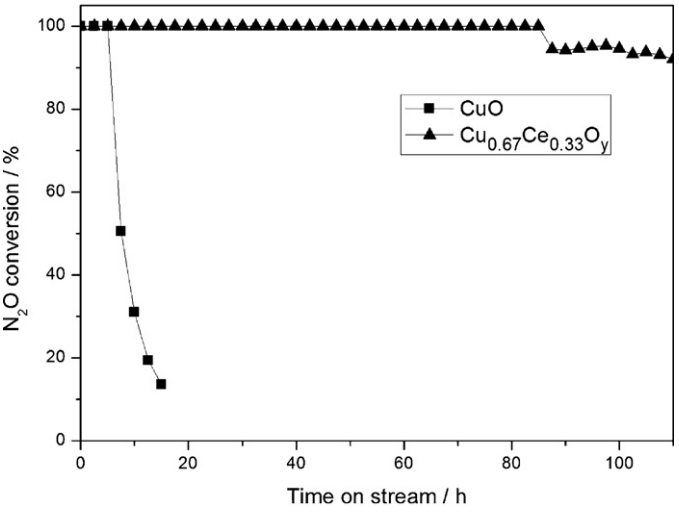

Fig. 8. Conversion of N_2O with time on stream at 480 °C over $Cu_{0.67}Ce_{0.33}O_y$, and CuO. Conditions: 2600 ppm N_2O, balance He, P = 0.3 MPa, GHSV = 19,000 h^{-1}.

3.4. Possible reaction mechanism over catalysts

Based on the results obtained so far, a possible reactions mechanism is proposed in Fig. 10. During the heating process, electron migration or oxygen migration occurs in the CuO–CeO_2 solid solution. Hence, Cu^{II} ions are reduced to Cu^I, and the synergic effect between Cu and Ce serves to stabilize Cu^I in the Structure II (Eqs. (1) and (2)) [27].

$$Cu^{II}\text{—}O\text{—}Ce^{III} \leftrightarrow Cu^{I}\text{—}O\text{—}Ce^{IV} \quad (1)$$

$$Cu^{II}\text{—}O + Ce^{III} \leftrightarrow Cu^{I} + O\text{—}Ce^{IV} \quad (2)$$

When cooled down to room temperature, the gas phase CO could coordinate to the stabilized Cu^I ions, and form the Cu^I–CO complexes showing a strong adsorbed signal at about 2100 cm^{-1} (Eq. (3)).

$$Cu^I + CO \rightarrow Cu^I\text{—}CO \quad (3)$$

On the other hand, the low valence state of Cu^I ions would arouse the coordination of N_2O on both O and N ends [24]. As for the case of

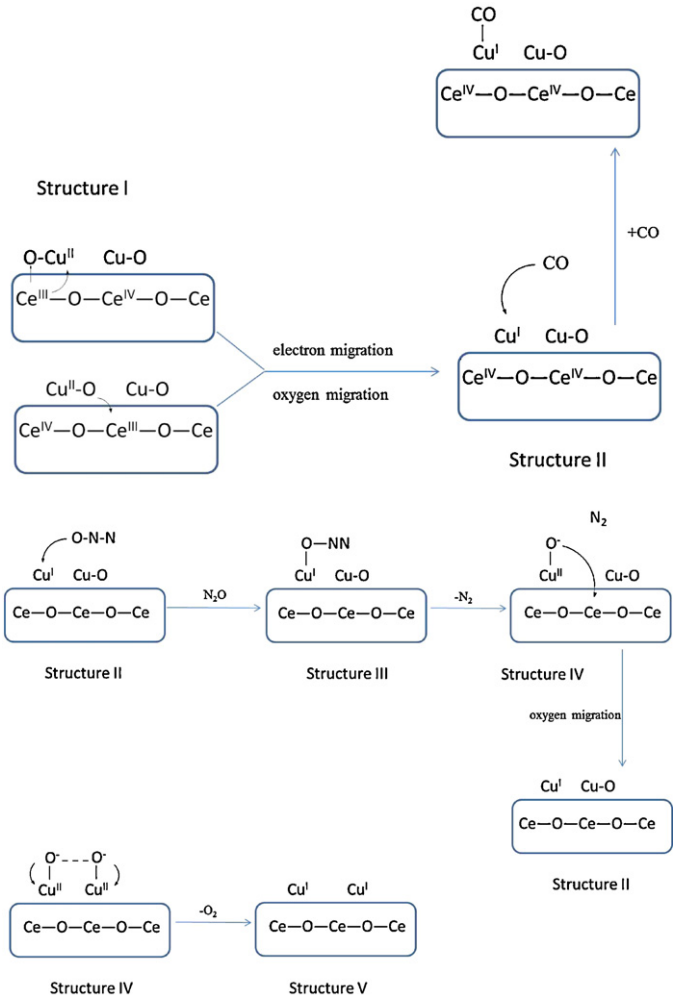

Fig. 10. The schematic diagram of CO interaction with copper oxide species, and the possible reaction mechanism for N_2O decomposition.

coordination on O end, the N—N bond order increases while weakening the N—O bond. The N-containing decomposition product is nitrogen. On the other hand, if coordination takes place on the N end, the N—O bond order between atoms increases and the N—N bond order decreases. Accordingly, the N-containing decomposition product is NO or NO_2. However, we have not yet detected such compounds in the DRIFTS study. As a result, N_2O deposits on the active Cu^I site only with the O atom (Eq. (4)).

$$Cu^I + N_2O \rightarrow Cu^I\text{—}ONN \quad (4)$$

In the next step, the weakened N—O bond breaks, releasing the gas phase N_2, at the same time, the active Cu^I species is oxidized to Cu^{II} (Eq. (5)).

$$Cu^I\text{—}ONN \rightarrow Cu^{II}\text{—}O^- + N_2 \quad (5)$$

After that, if two neighboring oxygen atoms are close enough, O_2 would form, and regenerate the active Cu^I (Eq. (6)).

$$2Cu^{II}\text{—}O^- \rightarrow 2Cu^I + O_2 \quad (6)$$

In addition, considering the high oxygen storage capacity of CeO_2, the oxidized active site could be regenerated in another way: the oxygen on the active site migrate to the Ce cation with the low valence state, regenerating the active Cu^I (Eq. (7)).

$$Cu^{II}\text{—}O^- + Ce^{III} \rightarrow Cu^I + Ce^{IV}\text{—}O^- \quad (7)$$

If the oxygen atom on the active site cannot be removed promptly, the catalyst deactivation occurs. The Structure III would return to the steady Structure II by oxygen migration.

In our view, the stability and the regeneration of Cu^I center are the key points in the reaction mechanism. The electron migration between Cu^I—O—Ce^{IV} and Cu^{II}—O—Ce^{III} ensures the stability of active site Cu^I, and the oxygen storage capacity of CeO_2 helps to regenerate the active site for further N_2O decomposition.

4. Conclusions

In this work, a series of $Cu_xCe_{1-x}O_y$ mixed oxides with different Cu/Ce molar ratios has been synthesized by citrate acid method. A noticeable synergy between CuO and CeO_2 has been observed for the activity in N_2O decomposition. Characterization of H_2-TPR, XPS and in situ DRIFTS results revealed that the synergetic effect between CuO and CeO_2 enhance the reducibility of copper species and promotes the formation of Cu^+, which accounts for the good catalytic performance for N_2O decomposition over $Cu_xCe_{1-x}O_y$ catalysts. The $Cu_{0.67}Ce_{0.33}O_y$ catalyst which possesses the largest amount of Cu^+ shows the best catalytic performance among all of the Cu-Ce-O catalysts.

Acknowledgments

This work was supported by the Chinese Ministry of Science and Technology, the “863” State Key Research Project (2009AA033701).

References

[1] M.H. Thiemens, W.C. Trogler, Science 251 (1991) 932–934.
[2] F. Kapteijn, J. RodriguezMirasol, J.A. Moulijn, Applied Catalysis B-Environmental 9 (1996) 25–64.
[3] J. Perez-Ramirez, F. Kapteijn, K. Schoffel, J.A. Moulijn, Applied Catalysis B-Environmental 44 (2003) 117–151.
[4] A. Dandekar, M.A. Vannice, Applied Catalysis B-Environmental 22 (1999) 179–200.
[5] X.D. Xu, H.L. Xu, F. Kapteijn, J.A. Moulijn, Applied Catalysis B-Environmental 53 (2004) 265–274.
[6] V.G. Komvokis, M. Marti, A. Delimitis, I.A. Vasalos, K.S. Triantafyllidis, Applied Catalysis B-Environmental 103 (2011) 62–71.
[7] E. Wilczkowska, K. Krawczyk, J. Petryk, J.W. Sobczak, Z. Kaszkur, Applied Catalysis A-General 389 (2010) 165–172.
[8] F.J. Perez-Alonso, I. Melián-Cabrera, M.L. Granados, F. Kapteijn, J.L.G. Fierro, Journal of Catalysis 239 (2006) 340–346.
[9] J.P. Dacquin, C. Lancelot, C. Dujardin, P. Da Costa, G. Djega-Mariadassou, P. Beaunier, S. Kaliaguine, S. Vaudreuil, S. Royer, P. Granger, Applied Catalysis B-Environmental 91 (2009) 596–604.
[10] J. Perez-Ramirez, F. Kapteijn, G. Mul, J.A. Moulijn, Chemical Communications (2001) 693–694.
[11] P.T. Fanson, M.W. Stradt, J. Lauterbach, W.N. Delgass, Applied Catalysis B-Environmental 38 (2002) 331–347.
[12] L. Xue, C.B. Zhang, H. He, Y. Teraoka, Applied Catalysis B-Environmental 75 (2007) 167–174.
[13] N. Pasha, N. Lingaiah, P.S.S. Reddy, P.S.S. Prasad, Catalysis Letters 127 (2009) 101–106.
[14] L.Z. Gao, C.T. Au, Applied Catalysis B-Environmental 30 (2001) 35–47.
[15] L.Z. Gao, C.T. Au, Journal of Molecular Catalysis A-Chemical 168 (2001) 173–186.
[16] P.J. Smeets, M.H. Groothaert, R.M. van Teeffelen, H. Leeman, E.J.M. Hensen, R.A. Schoonheydt, Journal of Catalysis 245 (2007) 358–368.
[17] P.E. Fanning, M.A. Vannice, Journal of Catalysis 207 (2002) 166–182.
[18] G. Avgouropoulos, T. Ioannides, H. Matralis, Applied Catalysis B-Environmental 56 (2005) 87–93.
[19] M.L. Fu, X.H. Yue, D.Q. Ye, J.H. Ouyang, B.C. Huang, J.H. Wu, H. Liang, Catalysis Today 153 (2010) 125–132.
[20] P. Djinovic, J. Batista, A. Pintar, Applied Catalysis A-General 347 (2008) 23–33.
[21] L. Xue, C.B. Zhang, H. He, Y. Teraoka, Catalysis Today 126 (2007) 449–455.
[22] M.F. Luo, J.M. Ma, J.Q. Lu, Y.P. Song, Y.J. Wang, Journal of Catalysis 246 (2007) 52–59.
[23] W. Liu, M. Flytzani-Stephanopoulos, Journal of Catalysis 153 (1995) 317–332.
[24] K. Asano, C. Ohnishi, S. Iwamoto, Y. Shioya, M. Inoue, Applied Catalysis B-Environmental 78 (2008) 242–249.
[25] H.L. Mai, D.S. Zhang, L.Y. Shi, T.T. Yan, H.R. Li, Applied Surface Science 257 (2011) 7551–7559.
[26] L.J. Liu, Z.J. Yao, B. Liu, L. Dong, Journal of Catalysis 275 (2010) 45–60.
[27] R.D. Zhang, W.Y. Teoh, R. Amal, B.H. Chen, S. Kaliaguine, Journal of Catalysis 272 (2010) 210–219.

[28] B.T. Qiao, A.Q. Wang, J. Lin, L. Li, D.S. Su, T. Zhang, Applied Catalysis B-Environmental 105 (2011) 103–110.
[29] J. Huang, L.C. Wang, Y.M. Liu, Y. Cao, H.Y. He, K.N. Fan, Applied Catalysis B-Environmental 101 (2011) 560–569.
[30] C. Morterra, E. Giamello, G. Cerrato, G. Centi, S. Perathoner, Journal of Catalysis 179 (1998) 111–128.
[31] M.V. Konduru, S.S.C. Chuang, Journal of Catalysis 196 (2000) 271–286.
[32] A.P. Jia, G.S. Hu, L. Meng, Y.L. Xie, J.Q. Lu, M.F. Luo, Journal of Catalysis 289 (2012) 199–209.
[33] A. Martinez-Arias, A.B. Hungria, M. Fernandez-Garcia, J.C. Conesa, G. Munuera, Journal of Physical Chemistry B 108 (2004) 17983–17991.
[34] Q. Yu, L.J. Liu, L.H. Dong, D. Li, B. Liu, F. Gao, K.Q. Sun, L. Dong, Y. Chen, Applied Catalysis B-Environmental 96 (2010) 350–360.
[35] L. Qi, Q. Yu, Y. Dai, C. Tang, L. Liu, H. Zhang, F. Gao, L. Dong, Y. Chen, Applied Catalysis B-Environmental 119–120 (2012) 308–320.
[36] L.J. Liu, B. Liu, L.H. Dong, J. Zhu, H.Q. Wan, K.Q. Sun, B. Zhao, H.Y. Zhu, L. Dong, Y. Chen, Applied Catalysis B-Environmental 90 (2009) 578–586.